

Observation of Incipient Charge Nematicity in $\text{Ba}(\text{Fe}_{1-x}\text{Co}_x)_2\text{As}_2$

Y. Gallais,^{1,*} R. M. Fernandes,² I. Paul,¹ L. Chauvière,¹ Y.-X. Yang,¹
M.-A. Méasson,¹ M. Cazayous,¹ A. Sacuto,¹ D. Colson,³ and A. Forget³

¹*Laboratoire Matériaux et Phénomènes Quantiques (UMR 7162 CNRS),
Université Paris Diderot-Paris 7, Bât. Condorcet, 75205 Paris Cedex 13, France*

²*School of Physics and Astronomy, University of Minnesota, Minneapolis, 55455, USA*

³*CEA-Saclay, IRAMIS, Service de Physique de l'Etat Condensé (SPEC URA CNRS 2464), F-91191 Gif-sur-Yvette, France*

Using electronic Raman spectroscopy, we report direct measurements of charge nematic fluctuations in the tetragonal phase of *strain-free* $\text{Ba}(\text{Fe}_{1-x}\text{Co}_x)_2\text{As}_2$ single crystals. The strong enhancement of the Raman response at low temperatures unveils an underlying charge nematic state that extends to superconducting compositions and which has hitherto remained unnoticed. Comparison between the extracted charge nematic susceptibility and the elastic modulus allows us to disentangle the charge contribution to the nematic instability, and to show that charge nematic fluctuations are weakly coupled to the lattice.

Electronic analogues of nematic states, in which rotational symmetry is broken but translational invariance is preserved, have been proposed in a variety of correlated materials [1], such as quantum Hall systems [2], cuprates [3, 4], ruthenates [5], heavy fermions [6] and, more recently, iron pnictide superconductors [7, 8]. In the latter, several experiments [7, 9–13] on strained samples have collected strong but indirect evidence that the tetragonal-to-orthorhombic structural transition is driven not by the lattice, but by electronic nematicity. However, these measurements could not disentangle the roles of the spin [14–17], charge and orbital [18–21] degrees of freedom in the nematic instability.

In $\text{Ba}(\text{Fe}_{1-x}\text{Co}_x)_2\text{As}_2$, the structural transition at T_s either precedes or accompanies a magnetic transition at T_N , disappearing near the doping concentration with the highest superconducting transition temperature T_c (see the phase diagram of Fig. 7(a)). The nematic/orthorhombic state is characterized by inequivalent Fe-Fe bond lengths along the in-plane a and b directions (x and y coordinates respectively of the one-Fe unit cell used throughout, see Fig. 7(a)), and by anisotropic electronic properties [7, 9, 12, 13, 22]. If this state is indeed a consequence of the condensation of an electronic nematic order parameter, its fluctuations should be present in the tetragonal phase and should increase as the temperature is lowered towards T_s . Probing these electronic nematic fluctuations directly is therefore fundamental to unveil the nature of the structural transition, and to evaluate their possible role in the superconducting pairing mechanism.

Here, we report electronic Raman scattering measurements of the charge nematic susceptibility in the tetragonal phase of $\text{Ba}(\text{Fe}_{1-x}\text{Co}_x)_2\text{As}_2$ single crystals in which no explicit tetragonal symmetry breaking stress was applied (i.e. strain-free crystals). We show that charge nematic fluctuations are manifested in the Raman spectra by a quasi-elastic peak in the $x^2 - y^2$ (B_{1g}) symmetry, whose intensity strongly increases in the tetragonal phase upon approaching T_s , signaling an incipient charge

nematic order. The extracted static charge nematic susceptibility displays a sizable enhancement over a wide doping range above the superconducting dome, suggesting it may play a role in the superconducting mechanism. Comparison with available shear modulus data indicates that the enhanced charge nematic susceptibility is weakly coupled to the lattice, highlighting the need to incorporate additional degrees of freedom to explain the structural transition.

Raman experiments have been carried out using a diode-pumped solid state laser emitting at 532 nm and a triple grating spectrometer equipped with a nitrogen cooled CCD camera [23]. Single crystals of $\text{Ba}(\text{Fe}_{1-x}\text{Co}_x)_2\text{As}_2$ were grown using the self-flux method. The magnetic and superconducting transition temperatures were determined by transport measurements performed on crystals from the same batch [24]. The structural transition temperature was determined by monitoring phonon anomalies observed when entering the orthorhombic phase [25].

The electronic Raman response, χ^μ , probes the weighted charge correlation function $\langle \rho^\mu(\omega) \rho^\mu(-\omega) \rangle$, where $\rho^\mu = \sum_{\mathbf{k}} \gamma_{\mathbf{k}}^\mu n_{\mathbf{k}}$ depends on the charge-density operator $n_{\mathbf{k}}$ of the momentum state \mathbf{k} , and on the form factor $\gamma_{\mathbf{k}}^\mu$ whose symmetry μ is determined by the polarizations \mathbf{e}_I and \mathbf{e}_S of the incident and scattered photons [1, 27]. To probe the in-plane charge nematic fluctuations, two polarization configurations can be considered (see inset of Fig. 7(d)). For photons polarized along the diagonals of the Fe-Fe bonds, the form factor has $x^2 - y^2$ (B_{1g}) symmetry, and is sensitive to nematic order along the Fe-Fe bonds. This is the type of C_4 (tetragonal) symmetry-breaking realized in the iron pnictides.

Note that while the charge nematic order parameter $\phi_{\mathbf{k}} \propto \gamma_{\mathbf{k}}^{x^2-y^2} n_{\mathbf{k}}$ changes sign under a 90° rotation, χ^μ is proportional to its square $\phi_{\mathbf{k}}^2$ and therefore is C_4 symmetric. Thus, unlike previous transport anisotropy measurements [7, 9, 11], we can extract the nematic fluctuations directly from the Raman response without applying any

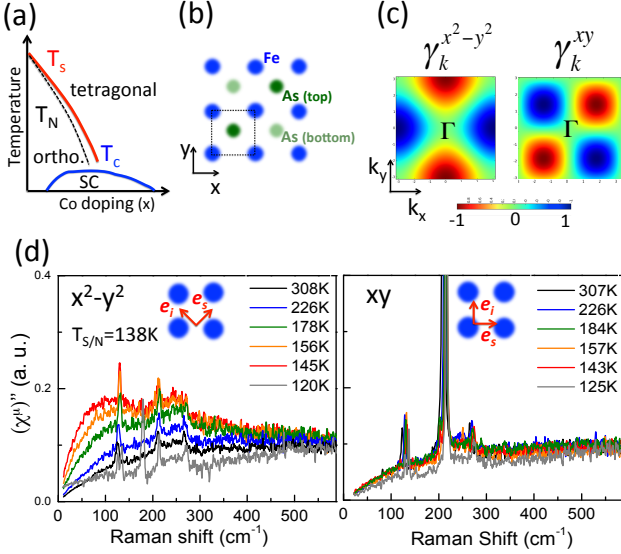


FIG. 1: (a), Sketch of the phase diagram of $\text{Ba}(\text{Fe}_{1-x}\text{Co}_x)_2\text{As}_2$. T_s , T_N and T_c are the structural, magnetic and superconducting (SC) transition temperatures respectively. (b), Tetragonal FeAs layer, with the x and y axes defined along the Fe-Fe bonds (c), Momentum-space structure of the form factor γ_k^μ for $x^2 - y^2$ and xy symmetries [27]. (d), Temperature dependent Raman response $(\chi^{x^2-y^2})''$ and $(\chi^{xy})''$ in a strain-free BaFe_2As_2 single crystal with $T_s = 138$ K. The incoming and outgoing photon polarizations ($\mathbf{e}_i, \mathbf{e}_s$) used for each symmetry configuration are depicted in the insets. The sharp peaks are due to phonon excitations. The electronic Raman continuum in $x^2 - y^2$ symmetry displays a low frequency quasi-elastic peak (QEP) that is superimposed on a weaker and broad continuum that extends to energies above 1000 cm^{-1} and is essentially temperature independent in the tetragonal phase (see supplemental Material [23]). In the orthorhombic phase, this broad continuum shows a suppression below 500 cm^{-1} in both symmetries because of the Fermi surface reconstruction induced by the simultaneous magnetic order [25].

external symmetry breaking field such as uniaxial stress. Besides the $x^2 - y^2$ (B_{1g}) symmetry, we also investigated the form factor with xy (B_{2g}) symmetry, which is insensitive to changes that make x and y inequivalent. The behaviors of these form factors in momentum space are depicted in Fig. 7(c).

Because of the fluctuation-dissipation theorem, the dynamic charge nematic fluctuations should be manifested in the imaginary part of the Raman response function $(\chi^\mu)''$ in the appropriate symmetry μ , namely, the $x^2 - y^2$ (B_{1g}) symmetry [28, 29]. This is illustrated in Fig. 7(d) for a strain-free, single crystal of the parent compound BaFe_2As_2 , where $(\chi^\mu)''$ is plotted as function of frequency for different temperatures and for the two symmetries described above. While the response in the xy symmetry is essentially temperature independent above $T_s = 138$ K, the $x^2 - y^2$ response displays a considerable build-

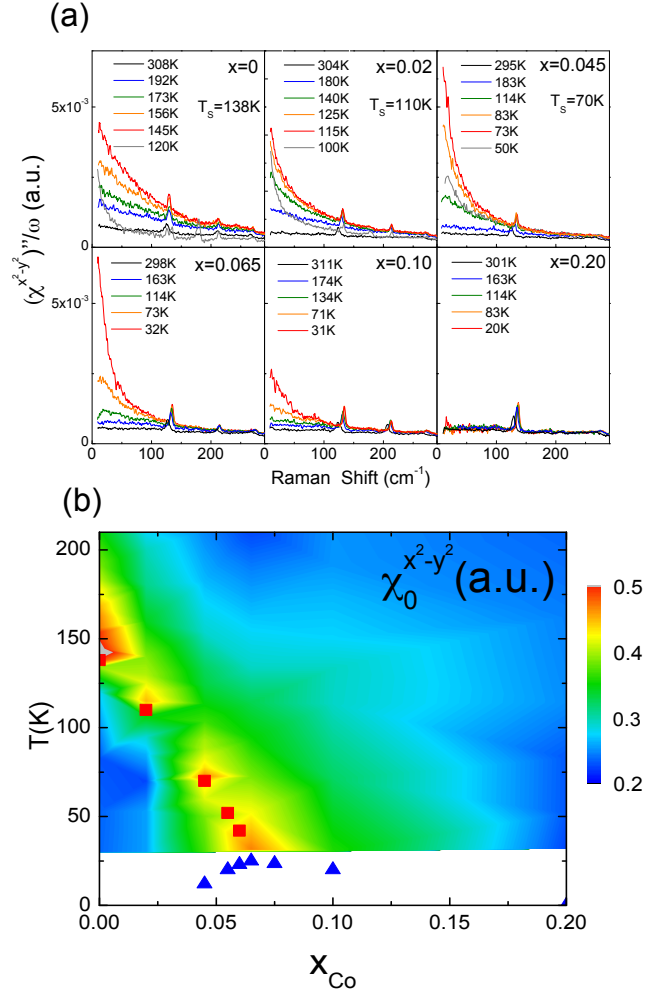


FIG. 2: (a), Temperature dependent Raman conductivity $(\chi^{x^2-y^2})''/\omega$ for $x = 0$ (parent), $x = 0.02$ (strongly underdoped), $x = 0.045$ (underdoped), $x = 0.065$ (optimally doped), $x = 0.10$ (overdoped), and $x = 0.20$ (strongly overdoped). The structural transition temperature is indicated for the three underdoped compositions. The $x = 0.065$ composition corresponds to optimal superconducting transition temperature ($T_c = 24.5 \text{ K}$) where no structural transition was detected. (b), Evolution of the static charge nematic susceptibility, $\chi_0^{x^2-y^2}$, as a function of temperature and doping. The structural transition temperature T_s and the superconducting transition temperature T_c are indicated in red squares and blue triangles respectively.

up of intensity below 500 cm^{-1} upon approaching T_s , with a subsequent collapse in the nematic/orthorhombic phase. The temperature dependence and the distinctive $x^2 - y^2$ symmetry of this low frequency quasi-elastic peak (QEP) clearly links it to dynamic charge nematic fluctuations corresponding to an orientational order along the Fe-Fe bonds. While the spectral line shape of the QEP is linked to the relaxational dynamics of the nematic fluctuations [30], we choose here to concentrate on a more transparent quantity: the static charge nematic suscep-

bility. Indeed the strong increase of the QEP intensity is associated with an enhanced static charge nematic susceptibility, $\chi_0^{x^2-y^2}$, via the Kramers-Kronig relation:

$$\chi_0^{x^2-y^2} = \frac{2}{\pi} \int_0^\infty d\omega (\chi''^{x^2-y^2}(\omega)/\omega) \quad (1)$$

The relevant quantity governing the static nematic susceptibility is thus the Raman conductivity χ''/ω , highlighting the importance of the low frequency part of χ'' in determining $\chi_0^{x^2-y^2}$. The temperature dependence of χ''/ω , where the QEP is now centered at zero frequency, is shown in Fig. 5(a) for six different Co concentrations of $\text{Ba}(\text{Fe}_{1-x}\text{Co}_x)_2\text{As}_2$, spanning the phase diagram from the parent $x = 0$ composition ($T_s = 138$ K and $T_c = 0$) up to the strongly overdoped $x = 0.20$ composition ($T_s = T_c = 0$). For $x \leq 0.045$, the QEP displays a systematic enhancement as temperature is lowered towards T_s before collapsing in the symmetry broken phase. The enhancement of the QEP extends down to T_c for $x = 0.065$ where the superconducting transition temperature is optimal and no structural transition is detected. For this particular composition the QEP was found to disappear quickly upon entering the superconducting state indicating a suppression of nematic fluctuations in the superconducting state (not shown). Above optimal composition, the enhancement of the QEP is strongly reduced but remains sizable even for $x = 0.10$, before disappearing for $x = 0.20$. The static charge nematic susceptibility $\chi_0^{x^2-y^2}$ was extracted using equation (9) via a partial integration of the Raman conductivity up to 500 cm^{-1} , since above this frequency the spectra are temperature independent in the tetragonal phase. To perform the integration, we used a Lorentzian relaxational form to extrapolate the Raman conductivity spectra from the lowest frequency experimentally accessible, 9 cm^{-1} , down to zero [23]. The doping and temperature dependence of $\chi_0^{x^2-y^2}$ are summarized in the phase diagram of Fig. 5(b). The maximum of the static charge nematic susceptibility closely tracks the structural transition temperature in the underdoped region, vanishing near optimal doping. This temperature and doping dependence is qualitatively consistent with previous anisotropic transport data of strained crystals [7, 9, 11]. However, resistivity anisotropy is only an indirect probe of the nematic order parameter since it cannot disentangle the various possible sources of electronic nematicity.

To perform a more quantitative analysis, in Fig. 3(a) we plot the inverse susceptibility as a function of temperature in the tetragonal phase ($T > T_s$) and for the six Co compositions. The softening of the inverse susceptibility, is seen for all compositions up to $x = 0.10$, being absent only for the strongly overdoped, non-superconducting, $x = 0.20$ composition. For all other compositions the inverse susceptibility above T_s can be well described over a large temperature range, spanning at least 150 K, by a

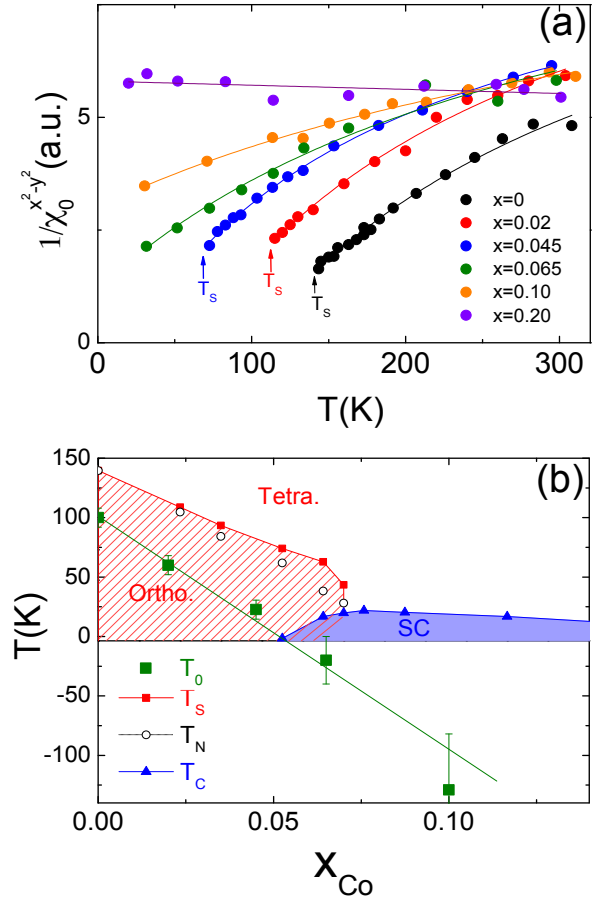


FIG. 3: (a), Temperature dependence of the inverse nematic charge susceptibility, $(\chi_0^{x^2-y^2})^{-1}$, in the tetragonal phase ($T > T_s$) as a function of Co composition. The lines are Curie-Weiss fits for each composition (see text). (b), (x, T) phase diagram showing the orthorhombic (Ortho.) and superconducting (SC) phases. The mean-field transition temperature extracted from the Curie-Weiss fit, T_0 , is shown in green square (the green line is a linear fit of its doping dependence). The corresponding structural transition temperature T_s (red squares), magnetic transition temperature T_N (white circles), and superconducting transition temperature T_c (blue triangles) are also indicated [24].

simple Curie-Weiss law of the form:

$$(\chi_0^{x^2-y^2})^{-1}(T) = \left(A + \frac{C}{T - T_0} \right)^{-1} \quad (2)$$

where A and C are constants and T_0 is the charge nematic transition temperature. The resulting fits for the inverse susceptibility are shown in Fig. 3(a). They unveil an incipient charge nematic instability at T_0 over a wide doping range, which includes the superconducting dome, in the phase diagram of $\text{Ba}(\text{Fe}_{1-x}\text{Co}_x)_2\text{As}_2$.

The extracted T_0 follows the trend of the thermodynamic structural transition temperature T_s , decreasing with doping and vanishing near $x \sim 0.06$. However, T_0 is significantly smaller than T_s , by about 50 K, across

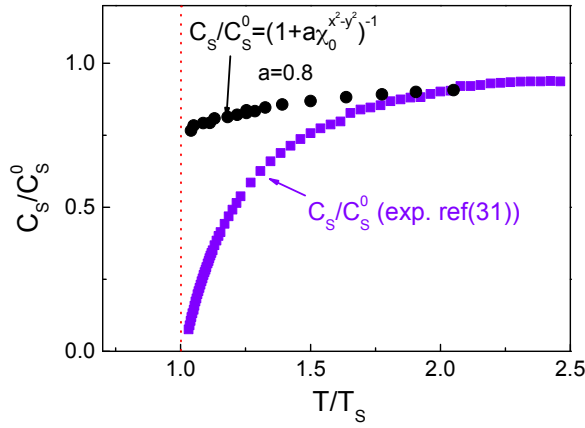


FIG. 4: Temperature dependence of the experimental shear modulus (data of Ref. [31], in purple), together with the expected temperature dependence of the shear modulus due to the coupling between the charge nematic and orthorhombic order parameters using Eq. (3) (in black). The bare shear modulus was assumed to be temperature independent and the only adjustable parameter, $a = \frac{\lambda^2}{C_s^0}$ (see text) was chosen to fit the shear modulus data at high temperatures ($a = 0.8$). The temperature scale was normalized using the measured structural transition temperatures ($T_s = 130\text{K}$ in Ref. [31]).

the entire phase diagram (see Fig. 3(b)). This fact, in conjunction with the observation of the build-up of the charge nematic fluctuations over a large temperature range, allow us to conclude that the incipient charge nematicity is not a mere consequence of the softening of the lattice orthorhombicity via a static linear coupling. More importantly, since the Curie-Weiss expression (2) with T_0 significantly smaller than T_s describes very well the data up to a few Kelvin above T_s , it implies that the incipient charge nematicity is, in fact, weakly coupled to the lattice. Because the tetragonal symmetry-breaking has to occur at the same temperature in both elastic and charge degrees of freedom, our analysis thus suggests the presence of another nematic degree of freedom which drives the structural transition at T_s .

We can also draw the same conclusions simply by comparing the $\chi_0^{x^2-y^2}$ data directly with the shear modulus $C_s \equiv C_{11} - C_{12}$, which measures the orthorhombic lattice stiffness [31, 32]. Since, by symmetry, the order parameters associated with C_s and $\chi_0^{x^2-y^2}$ are linearly coupled, we obtain

$$\frac{C_s}{C_s^0} = \left[1 + \left(\frac{\lambda^2}{C_s^0} \right) \chi_0^{x^2-y^2} \right]^{-1}, \quad (3)$$

provided charge nematicity is the only soft mode present [17, 31]. Here, λ is the linear coupling constant and C_s^0 is the high-temperature shear modulus. In Fig. 4, we test the validity of the above relation for the parent compound BaFe_2As_2 by comparing the C_s values inferred from our $\chi_0^{x^2-y^2}$ data via equation (3) (black) with the

experimental C_s data of Ref. [31] (purple). The discrepancy between the two confirms our inference above that charge nematicity is not the only soft mode, suggesting the presence of an additional electronic nematic degree of freedom. The precise nature of this additional degree of freedom cannot be ascertained from our Raman study. It is possible that spin fluctuations drive the softening of C_s [14–17] and $\chi_0^{x^2-y^2}$ via spin-lattice and spin-charge couplings, respectively. Alternatively, it has also been proposed that the structural transition is driven by orbital ordering between xz and yz Fe 3d orbitals [18–21]. Although the charge fluctuations measured here do not necessarily come only from fluctuations of the relative charge $n_{xz} - n_{yz}$ between these two orbitals, it follows from the orbital content of the Fermi surface of the iron pnictides that these orbital fluctuations should give a major contribution to $\chi_0^{x^2-y^2}$ if orbital order is the driving instability ([2], see also Supplemental Material [34]).

In conclusion, we presented electronic Raman spectroscopy study of $\text{Ba}(\text{Fe}_{1-x}\text{Co}_x)_2\text{As}_2$ single crystals in the tetragonal phase, where the C_4 symmetry is intact. Our analysis of the temperature dependence of the enhanced charge nematic susceptibility, and its comparison to the shear modulus data, indicate that although these fluctuations contribute to promote the breaking of the tetragonal symmetry, they are not the only driving mechanism behind it. The persistence of these fluctuations above the entire superconducting dome raises the question of whether they play a role in the pairing mechanism [22, 35]. Our results are reminiscent of earlier Raman studies indicating fingerprints of fluctuating charge density wave order in cuprates [28, 36]. We note however that in contrast to the stripe or checkerboard orders observed in cuprates, the fluctuating nematic order observed here does not break any lattice translational symmetry. Besides shedding light on the nature of the nematic state of the pnictides, our approach provides a novel route to investigate electronic nematicity in other strongly correlated systems where this type of state has been proposed.

We thank F. Rullier-Albenque for providing us with transport data. We acknowledge fruitful discussions with A. Chubukov, V. Keppens, D. Mandrus and J. Schmalian. Y.G., L.C., Y.X. Y., M.C, M.-A.M., A.S., D.C. and A.F. acknowledge support from Agence Nationale de la Recherche through Grant PNICTIDES.

* Electronic address: yann.gallais@univ-paris-diderot.fr

- [1] S. A. Kivelson, E. Fradkin and V. J. Emery, *Nature* **393**, 550 (1998).
- [2] M. P. Lilly, K. B. Cooper, J. P. Eisenstein, L. N. Pfeiffer and K. W. West, *Phys. Rev. Lett.* **82**, 394 (1999).
- [3] S. A. Kivelson, I. P. Blindloss, E. Fradkin, V. Oganesyan,

- J. M. Tranquada, A. Kapitulnik and C. Howald, *Rev. Mod. Phys.* **75**, 1201 (2003).
- [4] R. Daou, J. Chang, D. LeBoeuf, O. Cyr-Choinière, F. Laliberté, N. Doiron-Leyraud, B. J. Ramshaw, R. Liang, D. A. Bonn, W. N. Hardy and L. Taillefer, *Nature* **463**, 519 (2010).
- [5] R.A. Borzi, S. A. Grigera, J. Farrell, S. J. S. Lister, S. L. Lee, D. A. Tennant, Y. Maeno and A. P. Mckenzie, *Science* **315**, 214 (2007).
- [6] R. Okazaki, T. Shibauchi, H. J. Shi, Y. Haga, T. D. Matsuda, E. Yamamoto, Y. Onuki, H. Ikeda and Y. Mastuda *Science* **331**, 439 (2011).
- [7] J. -H. Chu, J. G. Analytis, K. De Greve, P. L. McMahon, Z. Islam, Y. Yamamoto, *Science* **329**, 824 (2010).
- [8] S. Kasahara, H. J. Shi, K. Hashimoto, S. Tonegawa, Y. Mizukami, T. Shibauchi, K. Sugimoto, T. Fukuda, T. Terashima, A. H. Nevidomskyy and Y. Matsuda, *Nature* **486**, 382 (2012).
- [9] M. A. Tanatar, E. C. Blomberg, A. Kreyssig, M. G. Kim, N. Ni, A. Thaler, S. L. Bud'ko, P. C. Canfield, A. I. Goldman, I. I. Mazin and R. Prozorov, *Phys. Rev. B* **81**, 184508 (2010).
- [10] T. M. Chuang, M. P. Allan, J. Lee, Y. Xie, N. Ni, S. L. Bud'ko, G. S. Boebinger, P. C. Canfield and J. C. Davis, *Science* **327**, 181 (2010).
- [11] J. -H. Chu, H.-H. Kuo, J. G. Analytis and I. R. Fisher., *Science* **337**, 710 (2012).
- [12] M. Yi, D. Lu, J. -H. Chu, J. G. Analytis, A. P. Sorini, A. F. Kemper, B. Moritz, S. -K. Mo, R. G. Moore, M. Hasimoto, W. -S. Lee, Z. Hussain, T. P. Devereaux, I. R. Fisher and Z.-X. Shen, *Proc. Natl Acad. Sci. USA* **108**, 6878 (2011).
- [13] A. Dusza, A. Lucarelli, F. Pfüner, J.-H. Chu, I. R. Fisher and L. Degiorgi, *EPL* **93**, 37002 (2011).
- [14] C. Fang, H. Yao, W.-F. Tsai, J. -P. Hu, and S. A. Kivelson, *Phys. Rev. B* **77**, 224509 (2008).
- [15] C. Xu, M. Muller and S. Sachdev, *Phys. Rev. B* **78**, 020501 (2008).
- [16] R. M. Fernandes, A. V. Chubukov, J. Knolle, I. Eremin and J. Schmalian, *Phys. Rev. B* **85**, 024534 (2012).
- [17] I. Paul, *Phys. Rev. Lett.* **107**, 047004 (2011).
- [18] C. C. Lee, W. -G. Yin and W. Ku, *Phys. Rev. Lett.* **103**, 267001 (2009).
- [19] C. C. Chen, J. Maciejko, A. P. Sorini, B. Moritz, R. R. P. Singh and T. P. Devereaux, *Phys. Rev. B* **82**, 100504 (2010).
- [20] W. Lv, F. Kruger, and P. Phillips, *Phys. Rev. B* **82**, 045125 (2010).
- [21] S. Onari and H. Kontani, *Phys. Rev. Lett.* **109**, 137001 (2012).
- [22] R.M. Fernandes, and J. Schmalian, *Supercond. Sci. Technol.* **25**, 084005 (2012).
- [23] see Supplementary Informations for details about the Raman experiments and the extraction of the static nematic charge susceptibility.
- [24] F. Rullier-Albenque, D. Colson, A. Forget and H. Alloul, *Phys. Rev. Lett.* **103**, 057001 (2009).
- [25] L. Chauvière, Y. Gallais, M. -A. Méasson, M. Cazayous, A. Sacuto, D. Colson and A. Forget, *Phys. Rev. B* **84**, 104508 (2011).
- [26] T. P. Devereaux and R. Hackl, *Rev. Mod. Phys.* **79**, 175 (2007).
- [27] see Supplemental Material for explicit expressions for the Raman form factors.
- [28] L. Tassini, F. Venturini, Q. -M. Zhang, R. Hackl, N. Kikugawa and T. Fujita, *Phys. Rev. Lett.* **95** 117002 (2005).
- [29] H. Yamase and R. Zeyher, *Phys. Rev. B* **83**, 115116 (2011). H. Yamase and R. Zeyher, *Phys. Rev. B* **88**, 125120 (2013).
- [30] see Supplemental Material for the an analysis of the functional form of the quasi-elastic peak.
- [31] R. M. Fernandes, L. H. VanBebber, S. Bhattacharya, P. Chandra, V. Keppens, D. Mandrus, M. A. McGuire, B. C. Sales, A. S. Sefat and J. Schmalian, *Phys. Rev. Lett.* **105**, 157005 (2010).
- [32] M. Yoshizawa, D. Kimura, T. Chiba, S. Simayi, Y. Nakanishi, K. Kihou, C. -H. Lee, A. Iyo, H. Eisaki, M. Nakajima, S. Uchida, *J. Phys. Soc. Jpn* **81**, 024604 (2012).
- [33] B. Valenzuela, M. J. Calderón, G. León and E. Bascones, *Phys. Rev. B* **87**, 075136 (2013).
- [34] see Supplemental Material for the correspondance between charge nematic and orbital fluctuations in iron pnictides.
- [35] H. Yamase and R. Zeyher, *Phys. Rev. B* **88**, 180502 (2013)
- [36] G. Blumberg, P. Littlewood, A. Gozar, B. S. Dennis, N. Motoyama, H. Eisaki and S. Uchida, *Science* **297**, 584 (2002)

Supplemental Material

I. RAMAN EXPERIMENTS

Raman experiments have been carried out using a diode-pumped solid state laser emitting at 532 nm and a triple grating spectrometer equipped with a nitrogen cooled CCD camera. In order to extract the imaginary part of the Raman response function, the raw spectra were corrected for the Bose factor and the instrumental spectral response. All temperatures were corrected for the estimated laser heating. It was first estimated by comparing the power and temperature dependences of the phonon frequencies. This estimate was then cross-checked by monitoring the onset of Rayleigh scattering by orthorhombic structural domains across the structural transition temperature as a function of laser power. Both methods yielded an estimated heating of $1 \text{ K} \pm 0.2$ per mW of incident power. In order to extract the imaginary part of the Raman response function, the raw spectra were corrected for the Bose factor and the instrumental spectral response.

II. EXTRACTION OF THE STATIC CHARGE NEMATIC SUSCEPTIBILITY FROM RAMAN SCATTERING MEASUREMENTS

The experimentally measured Raman intensity in the symmetry μ , $I^\mu(\omega)$, is proportional to the weighted charge correlation function $S^\mu(\omega)$.

$$I^\mu(\omega) \propto S^\mu(\omega) = \langle \rho^\mu(\omega) \rho^\mu(-\omega) \rangle \quad (4)$$

The correlation function S^μ is in turn directly linked to the imaginary part of the Raman response $(\chi^\mu)''$ via the fluctuation dissipation theorem:

$$S^\mu(\omega) = -\frac{\hbar}{\pi} (1 + n(\omega, T)) (\chi^\mu)''(\omega) \quad (5)$$

where $n(\omega, T)$ is the Bose-Einstein distribution function. The electronic Raman response function χ^μ is given by:

$$\chi^\mu(\omega) = \frac{i}{\hbar} \int_0^\infty dt e^{i\omega t} \langle [\rho^\mu(t), \rho^\mu(0)] \rangle \quad (6)$$

where the operator ρ^μ has the form

$$\rho^\mu = \sum_{\mathbf{k}} \gamma_{\mathbf{k}}^\mu n_{\mathbf{k}} \quad (7)$$

in terms of the charge density operator $n_{\mathbf{k}}$ in the momentum state \mathbf{k} , and a form factor, also called the Raman vertex, $\gamma_{\mathbf{k}}^\mu(\mathbf{e}_i, \mathbf{e}_s)$, whose symmetry index μ depends on

the polarizations of the incident and scattered lights \mathbf{e}_i and \mathbf{e}_s respectively. [1] Since the photon wave vector is several orders of magnitude smaller than the typical Brillouin zone size, there is negligible momentum transfer in the electron-photon scatterings, and therefore Raman spectroscopy probes the system uniformly.

The $x^2 - y^2$ or B_{1g} symmetry can be selected by choosing crossed incoming and outgoing photon polarizations at 45 degrees with respect to the Fe-Fe bonds. Here the notation B_{1g} refers to the one Fe unit cell whose axes are along the Fe-Fe bonds. Similarly the xy or B_{2g} symmetry can be selected by choosing incoming and outgoing photon polarizations along the Fe-Fe bonds. Note that in terms of the full lattice unit cell (or 4 Fe unit cell), which has its axes at 45 degrees to the Fe-Fe bonds and is more commonly used in the Raman literature, the B_{1g} (B_{2g}) symmetry discussed here corresponds to the B_{2g} (B_{1g}) symmetry.

The momentum space structure of $\gamma_{\mathbf{k}}^\mu$ is constrained by symmetry. For example in the case of $x^2 - y^2$ symmetry, $\gamma_{\mathbf{k}}^\mu$ must change sign under mirror symmetry with respect to the direction at 45 degrees of the x and y axis. Using the effective mass approximation for a tight binding model with nearest neighbour hopping integrals only we have $\gamma_{\mathbf{k}}^{x^2-y^2} = \cos k_x - \cos k_y$ and $\gamma_{\mathbf{k}}^{xy} = \sin k_x \sin k_y$ [1, 2]. The \mathbf{k} -space structure of these form factors are shown in Fig. 1 of the main manuscript.

While we only have access to the imaginary part of the symmetry dependent response as a function of frequency, we can extract the corresponding static susceptibility, χ_0^μ , using the Kramers-Kronig relation linking the real and the imaginary parts of the Raman response function:

$$\chi'(\omega) = \frac{1}{\pi} \int_{-\infty}^{\infty} d\omega' \frac{\chi''(\omega')}{\omega' - \omega} \quad (8)$$

Taking $\omega = 0$ and using the fact that χ'' is an odd function of ω , we obtain the following expression for the symmetry dependent static susceptibility:

$$\chi_0^\mu = \frac{2}{\pi} \int_0^\infty d\omega' (\chi^\mu)''(\omega') / \omega' \quad (9)$$

The expression above shows that the relevant quantity controlling the static susceptibility is not the Raman response χ'' but the Raman "conductivity" χ''/ω which is dominated by its low frequency behavior.

In terms of the generalized momentum-dependent charge nematic response function $\chi^\mu(\mathbf{q}, \omega)$, the above procedure is equivalent to taking the limit $\mathbf{q} \rightarrow \mathbf{0}$ first and then $\omega \rightarrow 0$. On the other hand the static nematic susceptibility, which diverges at a second order phase transition, is defined by the opposite order of limits where $\omega \rightarrow 0$ first and then $\mathbf{q} \rightarrow \mathbf{0}$. It is well-known that the order of limits is crucial for conserved quantities, for which the former way of taking limits give zero while the latter gives a finite value in thermodynamically stable phases.

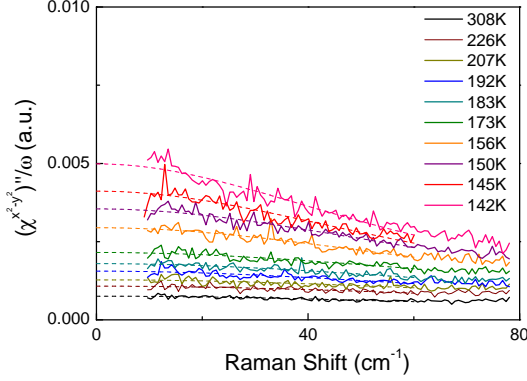


FIG. 5: Extrapolation of $(\chi^{x^2-y^2})''/\omega$ for $x = 0$ (parent compound BaFe_2As_2) and for 10 different temperatures in the tetragonal phase. The extrapolation was performed by fitting with a Lorentzian relaxational form the frequency window 9-25 cm^{-1} (see text).

It is important to note that the nematic charge operator defined in Eq. (7) is not a conserved quantity, and therefore the two limits can be interchanged.

Experimentally only the response in $x^2 - y^2$ symmetry, which measures charge nematic fluctuations, shows a significant build-up at low frequency or quasi-elastic peak (QEP) upon cooling. The QEP appears as a peak centered at zero-frequency in the raw intensity data, I , while it is pushed to finite frequency when the quantity χ'' is plotted as in the main manuscript (see Eq. (5)). Since we have only access to a finite frequency range, the integral in Eq. (9) can only be performed up to a finite frequency cut-off. Experimentally the QEP above T_s is superimposed on a weaker and broad electronic continuum that extends up to energies above 1000 cm^{-1} . This continuum shows a reconstruction in the SDW state [3] in both $x^2 - y^2$ and xy symmetries but is essentially temperature independent in the tetragonal phase. This suppression in the SDW state demonstrates a sizeable electronic Raman response in both symmetries, but the presence of nematic fluctuations in the $x^2 - y^2$ symmetry only.

In the tetragonal phase χ'' is to within our experimental accuracy temperature independent above 500 cm^{-1} in both symmetries. One can therefore reliably extract the temperature dependent charge nematic susceptibility by restricting the integral to energies lower than 500 cm^{-1} where the response is temperature dependent and dominated by the QEP. On the low energy side, the Raman measurements were performed down to 9 cm^{-1} . In order to perform the integration down to zero frequency, the Raman conductivity, $(\chi^{x^2-y^2})''(\omega')/\omega'$ was extrapolated assuming a Lorentzian relaxational form for the Raman conductivity at low frequency:

$$(\chi^{x^2-y^2})''(\omega)/\omega \sim \frac{\Gamma}{\Gamma^2 + \omega^2} \quad (10)$$

where Γ is a static relaxation rate. The extrapolations are shown in Fig. 5. The resulting static nematic susceptibility is shown as a function of temperature and doping in Fig. 2 of the manuscript.

III. MODELING OF THE QUASI-ELASTIC PEAK USING A LORENTZIAN RELAXATIONAL FORM

The data in $x^2 - y^2$ symmetry channel can be modeled using a temperature independent background of the same shape as the one seen in the xy symmetry channel plus a quasi-elastic peak (QEP) which has the functional form of a Lorentzian relaxation with a scattering rate Γ :

$$(\chi^{x^2-y^2})'' \sim \frac{\omega\Gamma}{\Gamma^2 + \omega^2} \quad (11)$$

This analysis is shown in figure 6(a),(b) below for $x=0$. The data in the tetragonal phase are well reproduced by this modeling for all temperatures. One advantage of this analysis is that it allows one to extract the spectral weight of the QEP only: the background-free diverging part of the charge nematic susceptibility $\chi_0^{x^2-y^2}$. One drawback however, is that the nematic susceptibility can only be reliably extracted when the QEP intensity is sizable, i.e. close to T_s , in our case between T_s and $T_s + 100\text{K}$ approximately. Outside this temperature range the fits and the resulting analysis are too dependent on the exact lineshape of the background that is subtracted.

The inverse susceptibility extracted with this method is shown in figure 6(c). It follows reasonably well a linear (i.e. Curie-Weiss) behavior at least for $x=0$, $x=0.02$, $x=0.045$ and $x=0.065$ compositions: $(\chi_0^{x^2-y^2})^{-1} \sim T - T_0$. This is fully consistent with the analysis reported in the main text where the total susceptibility (background plus QEP) was fitted with a constant plus a Curie Weiss term (see Eq. (2) of the main text). Besides, as shown in figure 6(d) the extracted temperature T_0 from the linear fits agrees within error bars with the one extracted from the analysis performed in the main text.

IV. POLARIZATION RESOLVED SPECTRA FOR $x = 0.02$

We show in fig. 7 the full polarization resolved Raman spectra for $x=0.02$ at $T=115\text{K}$. The four polarization configurations include the two crossed polarization configurations introduced in the manuscript (B_{1g} or $x^2 - y^2$ symmetry, and xy or B_{2g} symmetry) along with

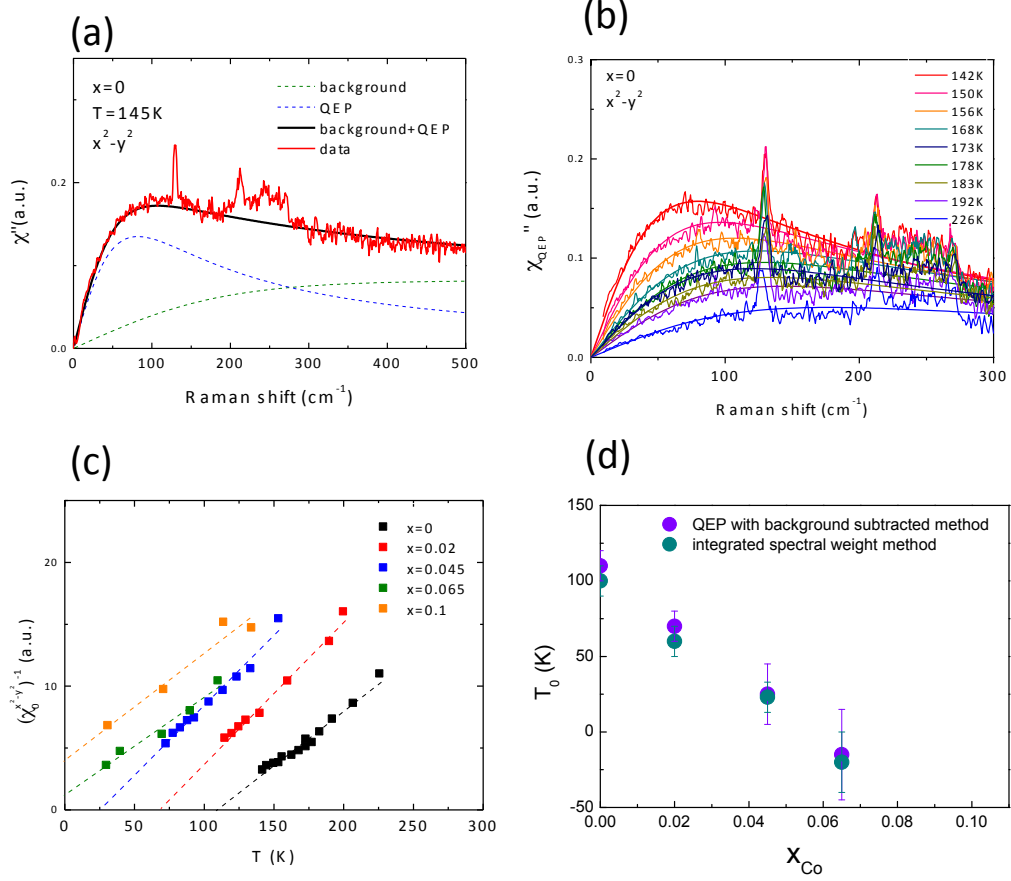


FIG. 6: (a): decomposition of the Raman spectrum in $x^2 - y^2$ symmetry using a broad continuum and a Lorentzian QEP. The broad continuum was taken so as to fit the xy continuum in the tetragonal phase. (b): fits of the background subtracted QEP as a function of temperature for $x=0$ using the Lorentzian relaxational form described in the text. (c): extracted inverse nematic susceptibility by integrating only the extracted diverging QEP part of the Raman conductivity for $x = 0$, $x = 0.02$, $x = 0.045$, $x = 0.065$ and $x = 0.1$. The inverse susceptibility shows linear Curie-Weiss-like behavior. T_0 corresponds to the temperature at which the inverse susceptibility extrapolates to zero. (d): x dependence of T_0 extracted from this analysis (in purple) and from the analysis described in the main text (in green). The T_0 values agrees with 10 percent.

the two parallel polarizations configurations which probe the $A_{1g}+B_{1g}$ and the $A_{1g}+B_{2g}$ symmetries of the tetragonal lattice structure. All symmetries show a sizable continuum that extends to energies above 500 cm⁻¹ but the temperature dependent low energy spectral weight due to the quasi-elastic peak is only seen in the two configurations (red and orange) which probe the B_{1g} or $x^2 - y^2$ symmetry.

V. RAMAN VERTEX IN THE ORBITAL BASIS

In a multi-orbital system, the basic operator for Raman response in the symmetry channel μ is given by:

$$\rho^\mu = \sum_{\mathbf{k}\sigma} \sum_{m,n} \gamma_{mn}^\mu(\mathbf{k}) c_{m,\mathbf{k}\sigma}^\dagger c_{n,\mathbf{k}\sigma} \quad (12)$$

where $c_{m,\mathbf{k}\sigma}^\dagger$ creates an electron with momentum \mathbf{k} and spin σ in orbital m . For the $x^2 - y^2$ channel, ignoring

screening effects and vertex corrections, the free-electron form factor or Raman vertex depends only on the band dispersion $\varepsilon_{mn}(\mathbf{k})$:

$$\gamma_{mn}^{x^2-y^2}(\mathbf{k}) = \frac{\partial^2 \varepsilon_{mn}(\mathbf{k})}{\partial k_x^2} - \frac{\partial^2 \varepsilon_{mn}(\mathbf{k})}{\partial k_y^2} \quad (13)$$

In the iron pnictides, all 3d orbitals may contribute to the Fermi surface. Let us focus on the role played by the orbitals xz and yz . In the tetragonal phase, their intra-orbital dispersions are identical upon a 90° rotation of the coordinate system, i.e.

$$\varepsilon_{xz,xz}(k_x, k_y) = \varepsilon_{yz,yz}(-k_y, k_x) \quad (14)$$

Therefore, it follows for the intra-orbital Raman vertices:

$$\gamma_{xz,xz}^{x^2-y^2}(k_x, k_y) = -\gamma_{yz,yz}^{x^2-y^2}(-k_y, k_x) \quad (15)$$

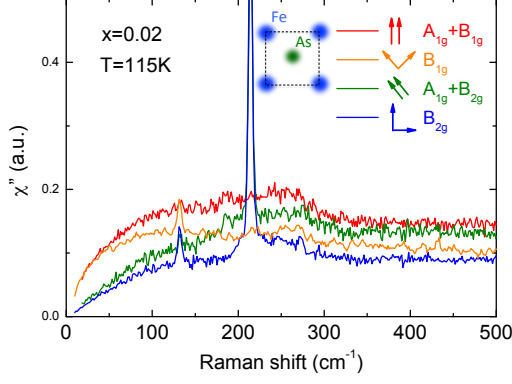


FIG. 7: Raman spectra in four polarization configurations for the $x = 0.02$ composition ($T_s = 110K$) and at $T = 115K$. For each configuration, the polarizations of the incoming and outgoing photons are sketched with respect to the Fe-As plane. The symmetries indicated correspond to the 1 Fe unit cell.

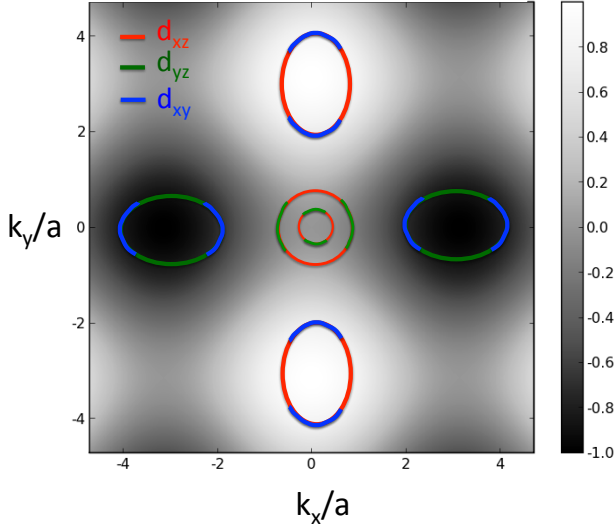


FIG. 8: $x^2 - y^2$ form factor ($\cos k_x - \cos k_y$) in grey scale. A sketch of the typical Fermi surface sheets of the iron pnictides has been superimposed [4]. Their orbital content is also indicated.

At low energies, the main contribution to the Raman scattering comes from electronic states at the Fermi level. Symmetry requires that if a point (k_x, k_y) at the Fermi surface has xz orbital character, then the point at $(-k_y, k_x)$ also belongs to the Fermi surface and has yz orbital character. Combined with the symmetry rela-

tion (15), this implies that the charge density difference $\delta n \equiv n_{xz} - n_{yz}$, with the proper overall form factor, contributes to the effective $x^2 - y^2$ Raman charge.

Similar conclusions can be drawn by analyzing the orbital content of the Fermi surface of the iron pnictides and the $x^2 - y^2$ form factor $\cos k_x - \cos k_y$. In Fig. 8, we superimpose a sketch of the typical Fermi surface of the iron pnictides to the form factor plotted in Fig. 1(c) of the main text. It is clear that the form factor changes sign between the electron pockets located at $X = (\pi, 0)$ and $Y = (0, \pi)$. First principle calculations [4] reveal that while the X electron pocket has mostly d_{yz} character (and no d_{xz} contribution), the Y pocket has mostly d_{xz} character (and no d_{yz} contribution). Therefore, since the $x^2 - y^2$ form factor changes sign between the X and Y pockets, and they have symmetry-related d_{xz} and d_{yz} spectral weights, the relative charge δn between the d_{xz} and d_{yz} orbitals appears in the $x^2 - y^2$ response.

Notice that the remaining $3d$ orbitals, as well as inter-orbital terms, in principle, also contribute to the $x^2 - y^2$ Raman response. A detailed discussion of all the non-zero intra-orbital and inter-orbital Raman vertices $\gamma_{mn}^\mu(\mathbf{k})$ was presented in Ref. [2]. For instance, the xy intra-orbital vertex also satisfies the relationship:

$$\gamma_{xy,xy}^{x^2-y^2}(k_x, k_y) = -\gamma_{xy,xy}^{x^2-y^2}(-k_y, k_x) \quad (16)$$

implying that a breaking of tetragonal symmetry could in principle be driven solely by the xy orbital. However, if the nematic instability is driven by a spontaneous d_{xz}/d_{yz} orbital polarization, as suggested by a few theoretical models, then the fluctuations associated with the charge density difference δn between xz and yz orbitals $\langle \delta n \delta n \rangle$ should dominate the $x^2 - y^2$ Raman susceptibility.

* Electronic address: yann.gallais@univ-paris-diderot.fr

- [1] T. P. Devereaux and R. Hackl, Rev. Mod. Phys. **79**, 175 (2007)
- [2] B. Valenzuela, M. J. Calderón, G. Leòn and E. Bascones, Phys. Rev. B **87**, 075136 (2013).
- [3] L. Chauviere, Y. Gallais, M. -A. Méasson, M. Cazayous, A. Sacuto, D. Colson and A. Forget, Phys. Rev. B **84**, 104508 (2011)
- [4] S. Graser, T. A. Maier, P. J. Hirschfeld, D. J. Scalapino, New J. Phys. **11**, 025016 (2009)